Research Article Vol. 12, No. 10 / 1 Oct 2021 / *Biomedical Optics Express* 6674

Biomedical Optics EXPRESS

Polarimetric visualization of healthy brain fiber tracts under adverse conditions: *ex vivo* studies

OMAR RODRÍGUEZ-NÚÑEZ,[1] PHILIPPE SCHUCHT,[2] EKKEHARD HEWER,[3] TATIANA NOVIKOVA,[1,*] AND ANGELO PIERANGELO[1]

[1] *LPICM, CNRS, Ecole polytechnique, IP Paris, Palaiseau, 91128, France*
[2] *Department of Neurosurgery, Inselspital, Bern University Hospital, University of Bern, 3010, Bern, Switzerland*
[3] *Lausanne University Hospital and University of Lausanne, 1011 Lausanne, Switzerland*
[*] *tatiana.novikova@polytechnique.edu*

Abstract: We suggest using the wide-field imaging Mueller polarimetry to contrast optically anisotropic fiber tracts of healthy brain white matter for the detection of brain tumor borders during neurosurgery. Our prior studies demonstrate that this polarimetric imaging modality detects correctly the in-plane orientation of brain white matter fiber tracts of a flat formalin-fixed thick brain specimen in reflection geometry [IEEE Trans. Med. Imaging **39**, 4376 (2020)]. Here we present the results of *ex vivo* polarimetric studies of large cross-sections of fresh calf brain in reflection geometry with a special focus on the impact of the adverse measurement conditions (e.g. complex surface topography, presence of blood, etc.) on the quality of polarimetric images and the detection performance of white matter fiber tracts and their in-plane orientation.

1. Introduction

Standard treatment for gliomas includes surgical resection, radiation and pharmacotherapy. According to the AWMF guidelines [1] for clinical decision-making, complete resection of the enhancing tumor should be attempted as the first-line therapy in patients with high grade gliomas. Planning of a complete resection depends on localization of the tumor and the neurological function of the surrounding tissue, as well as suspected entity and dignity of the tumor. For low-grade tumors, a complete resection should be attempted. During white-light microscopy-assisted neurosurgery it is often impossible to differentiate the tumor tissue from the healthy tissue in the border zone.

Hence, non-invasive identification of tumor tissue during surgery for safe and complete tumor excision remains a major challenge in neurosurgery. The failure to identify tumor tissue during surgery is a risk factor for incomplete resection, and hence poorer prognosis [2,3]. Post-operative neurological deficits related to the excessive resection of infiltrated brain tissue have devastating effects on a patient's quality of life and survival time, and still occur in >10 % of surgeries for intrinsic brain tumors according to contemporary series [4,5].

Intra-operative identification of specific, crucial fiber tracts, such as the cortico-spinal tract or the arcuate fascicle fiber tracts during open brain surgery is of particular interest to the neurosurgeon. It is mainly performed by using pre-operative, fiber tract based MRI-navigation and intra-operative electrophysiology (IOM) [6–9]. However, MRI-navigation is known to loose accuracy during surgery [10]. IOM is only available in a reliable manner for motor function, and for speech, for which the patient needs to be woken up in mid-surgery with all drawbacks that this entails. The pre-operative oral administration of 5-aminolevulinic acid (5-ALA) helps to visualize high-grade gliomas during neurosurgery [11,12]. However, the fluorescence imaging technique has the limitations related to the insufficient accumulation of protoporphyrin IX in low-grade gliomas or metastases.

#439754 https://doi.org/10.1364/BOE.439754
Journal © 2021 Received 5 Aug 2021; revised 22 Sep 2021; accepted 22 Sep 2021; published 1 Oct 2021
Corrected: 14 Oct 2021

The ability to identify fiber tracts non-invasively and in real time in the tissue-at-sight would be a breakthrough for brain tumor surgery. With the well-known location and course of the brain‘s main fiber tracts in mind the surgeon would be able to identify the fiber tracts in his/her field of view thanks to their in-plane spatial orientation. This ability would be a significant addition to existing techniques. For instance, if baseline testing is too poor or if compliance of a patient becomes too low during speech mapping, fiber identification would allow the surgeon to identify and preserve the arcuate fascicle. Other tracts, which surgeons cannot reliably identify during surgery at present, such as the visual pathway, could be identified and spared.

Optical imaging has already become a reliable technique for medical diagnostics. The classical intensity images taken with either an endoscope or a binocular microscope provide visual information about the biological tissue, such as its color, vascularization, surface texture, presence of lesions, etc. For example, these imaging modalities are routinely used for the characterization of superficial tissue layers in gynecology, dermatology, stomatology, ophthalmology and gastroenterology [13–17]. Confocal microscopy and optical coherence tomography (OCT) techniques make use of ballistic (non-scattered) photons to produce the microscopic depth-resolved images. For both modalities the acquired images provide very detailed information on a micrometer scale about the structure of explored tissue. However, their field of view is typically less than a few square millimeters, and their penetration depth does not exceed a few hundred microns [18,19]. One can also analyze spectrally and/or angularly light scattered by a sample in order to extract information about the size and density of scatterers, as well as the absorption or fluorescence properties of a sample [20]. For these techniques the penetration depth of light may be significantly greater compared to OCT or confocal imaging, but they do not provide the image of a sample.

However, optics may offer the complementary dataset by exploring the polarization of light, which represents its fundamental property [21] and is known to be extremely sensitive to the microstructure of the illuminated object. The non-exhaustive list of optical techniques that measure changes of the polarization state of incident light induced by its interaction with the sample includes, for example, polarized light microscopy, orthogonal state contrast measurements, ellipsometry, Stokes polarimetry, and complete Mueller polarimetry [22–30].

Quite often biological tissues exhibit significant depolarization. Sometimes the depolarization is combined with other changes in polarimetric properties such as birefringence (anisotropy of the refractive index) and diattenuation (anisotropy of the absorption). Hence, the most complete polarimetric technique, (i.e. Mueller polarimetry) is required for the characterization of tissue’s optical properties for biomedical diagnosis [31]. White matter of healthy brain has highly ordered architecture due to the presence of densely packed nerve fiber bundles (or fiber tracts) that are destroyed by brain tumor. The ability to identify fibers as a surrogate marker for healthy brain tissue enables the surgeon to identify brain tumors, simply by the former‘s lack of aligned fibers.

We suggest using the multi-spectral wide-field imaging Mueller polarimetry (IMP) for the visualization of healthy brain fiber tracts by measuring the depolarization and birefringence of brain tissue without scanning [32]. In our study we investigated the capability of the IMP to detect the fiber tracts of a fresh calf brain under the adverse measurement conditions that mimic the constrains of *in vivo* polarimetric measurements during neurosurgery (complex surface topography, presence of blood, etc).

2. Materials and methods

2.1. Stokes-Mueller formalism

In the framework of linear optics one may use the Jones formalism that describes the transformation of the complex amplitudes of electric field vector of polarized light by its interaction with a sample. However, more general Stokes-Mueller formalism makes use of the second moments of the distributions of electric field amplitudes (i. e. intensities of light) and may be used for the description of polarized, partially polarized as well as unpolarized light [21]. We define the Stokes vector of a light beam as

$$\mathbf{S} = \begin{bmatrix} S_1 \\ S_2 \\ S_3 \\ S_4 \end{bmatrix} = \begin{bmatrix} I_{0^\circ} + I_{90^\circ} \\ I_{0^\circ} - I_{90^\circ} \\ I_{+45^\circ} - I_{-45^\circ} \\ I_R - I_L \end{bmatrix} \tag{1}$$

where I_{0° and I_{90° are the intensities of horizontal and vertical linear polarization, respectively. I_{+45° and I_{-45° represent the intensity of linear polarization at the angles +45° and −45°, I_R and I_L are the intensities of right- and left-handed circularly polarized light.

Upon interaction with a sample the transformation of Stokes vector of incident light $\mathbf{S}^{in}$ is described by a 4×4 real-valued matrix $\mathbf{M}$ [21], called the Mueller matrix (MM) of a sample.

$$\begin{bmatrix} S_1^{out} \\ S_2^{out} \\ S_3^{out} \\ S_4^{out} \end{bmatrix} = \begin{bmatrix} M_{11} & M_{12} & M_{13} & M_{14} \\ M_{21} & M_{22} & M_{23} & M_{24} \\ M_{31} & M_{32} & M_{33} & M_{34} \\ M_{41} & M_{42} & M_{43} & M_{44} \end{bmatrix} \begin{bmatrix} S_1^{in} \\ S_2^{in} \\ S_3^{in} \\ S_4^{in} \end{bmatrix} \tag{2}$$

Mueller matrix $\mathbf{M}$ contains all information on polarimetric properties of a sample, whereas the physical interpretation of each Mueller matrix element is not always straightforward. By measuring all 16 elements of a MM and applying an appropriated decomposition method a complete set of relevant polarization and depolarization parameters (e. g. dichroism, polarizance, retardance, depolarization, etc.) can be obtained [33].

2.1.1. Wide-field imaging Mueller polarimetric system

A custom-built multi-spectral wide-field imaging Mueller polarimetric system used in these studies is described in details elsewhere [34–37]. For the sake of completeness we recall the main specifications of the instrument here. It makes use of ferroelectric liquid crystals (FLCs) for the fast polarization modulation and can record 16 raw intensity images of a sample in 5 seconds. The system operates in a visible wavelength range (450 nm - 700 nm). The construction and optimization of such a system is described in [38]. The photo and schematic of the instrument are presented in Fig. 1.

The polarization state generator (PSG) represents a sequential assembly of a linear polarizer and two voltage-driven FLCs (Citizen Finetech Miyota, Japan) with a quarter-wave plate inserted between them. The polarization state analyser (PSA) is made of the same optical elements, but assembled in a reverse order. A xenon lamp is used as the source of incoherent white light. Each FLC operates as a wave plate with constant retardation and switchable orientation of the optical axis at either 0° or 45°. The angle of incidence is about 15°, the beam is slightly divergent. Maximal dimension of the elliptical spot in the imaging plane is about 10 cm. The light scattered by a sample passes through the PSA and one of the 40 nm bandpass interference filters (with a central wavelength varying from 450 to 700 nm in steps of 50 nm) that are placed in a rotating wheel for performing spectral measurements. We use a CCD camera (Stingray F080B, Allied Vision, Germany, resolution 512 × 386 pixels) for recording the intensity images. Camera's optical axis is placed normal to the sample imaging plane. The use of the wide bandpass dichroic filters helps to increase the signal to noise ratio and to erase the speckle pattern. The reference calibration samples (two polarizers with the eigenaxes oriented at 0° and 90°, respectively, and a wave plate with the fast axis oriented at 30° in the laboratory reference frame) are placed in

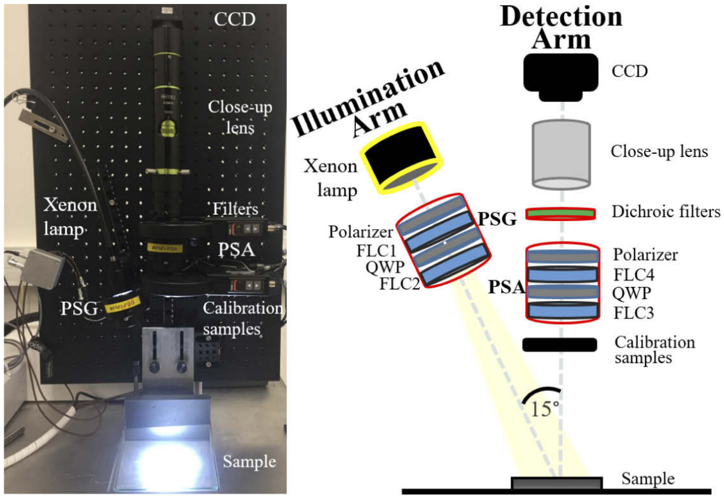

Fig. 1. A wide-field imaging Mueller polarimeter operating at multiple wavelengths in the visible wavelength range. Photo of the instrument (left panel) and the schematic optical layout (right panel). The PSG consists of a linear polarizer oriented at 0° with respect to the laboratory reference frame, followed by a first ferroelectric liquid crystal (FCL1), a quarter-wave plate (QWP) and a second ferroelectric liquid crystal (FLC2). The PSA is made up of the same components in reverse order compared to PSG configuration.

a rotating wheel before the PSA. The optimal PSG and PSA polarization states are defined by the eigenvalue calibration method [39]. The acquisition of 16 intensity images for four different input and four different output polarization states is performed sequentially at each measurement wavelength. The MM of a sample is calculated pixel-wise from the raw intensity images [39] taken at each measurement wavelength.

2.1.2. Lu-Chipman decomposition of Mueller matrix

Lu-Chipman polar decomposition of MM represents the algorithm of a non-linear compression of polarimetric data. It was demonstrated that any physically realizable MM can be represented as the product of MMs of three basic optical elements, namely, diattenuator ($\mathbf{M}_D$), retarder ($\mathbf{M}_R$) and polarizing depolarizer ($\mathbf{M}_\Delta$) [33]:

$$\mathbf{M} = \mathbf{M}_\Delta \mathbf{M}_R \mathbf{M}_D \tag{3}$$

$$\mathbf{M}_D = T_u \begin{bmatrix} 1 & \mathbf{D}^T \\ \mathbf{D} & \mathbf{m}_D \end{bmatrix}, \mathbf{M}_R = \begin{bmatrix} 1 & \mathbf{0}^T \\ \mathbf{0} & \mathbf{m}_R \end{bmatrix}, \mathbf{M}_\Delta = \begin{bmatrix} 1 & \mathbf{0}^T \\ \mathbf{P} & \mathbf{m}_\Delta \end{bmatrix} \tag{4}$$

and T_u denotes the transmittance (or reflectance) for unpolarized light, $\mathbf{D}$ - 3×1 vector of diattenuation, $\mathbf{P}$ - 3×1 vector of polarizance, $\mathbf{m}_D$, $\mathbf{m}_R$ and $\mathbf{m}_\Delta$ - real-valued 3×3 matrices.

The matrix product does not commute, so the sequential order of the appearance of polarimetric effects is fixed for this decomposition algorithm. The total depolarization is calculated as

$$\Delta = 1 - \frac{|tr(\mathbf{M}_\Delta - 1)|}{3}, \quad 0 \leq \Delta \leq 1 \tag{5}$$

The combined effect of linear and circular birefringence is defined as

$$R_{LC} = \cos^{-1}\left(\frac{tr(\mathbf{M}_R)}{2} - 1\right) \tag{6}$$

$\mathbf{M}_R$ can be expressed as a combination of a Mueller matrix of linear retarder with the linear retardance R and the azimuth of the optical axis φ and a Mueller matrix of a circular retarder with optical rotation angle ψ [40]. These parameters are calculated as

$$R = \cos^{-1}\left(\sqrt{(M_R(2,2) + M_R(3,3))^2 + (M_R(3,2) - M_R(2,3))^2} - 1\right) \tag{7}$$

$$\varphi = 0.5\tan^{-1}\left(\frac{M_R(2,4)}{M_R(4,3)}\right), \tag{8}$$

$$\psi = \tan^{-1}\left(\frac{M_R(3,2) - M_R(2,3)}{M_R(2,2) + M_R(3,3)}\right) \tag{9}$$

We have focused our studies on the images of the total depolarization coefficient Δ, and the azimuth φ of the optical axis of linear birefringent medium, because both images demonstrate useful contrast for the visualization of brain white matter fiber tracts.

2.1.3. Brain samples

Fresh calf brain samples (aka cervelle de veau) were bought from a local French butcher the day of the experiment. The brain samples were not rinsed with water in order to perform the polarimetric measurements on fresh brain tissues that contain blood residual.

3. Results and discussion

3.1. Depolarization mask for filtering polarimetric images of brain

The images of 3 cm × 3 cm section of cerebellum [41] of a fresh calf brain are shown in Fig. 2. The polarimetric images of brain tissue namely, depolarization and the azimuth of the optical axis were obtained by applying pixel-wise the Lu-Chipman polar decomposition (Eqs. (3)–7).

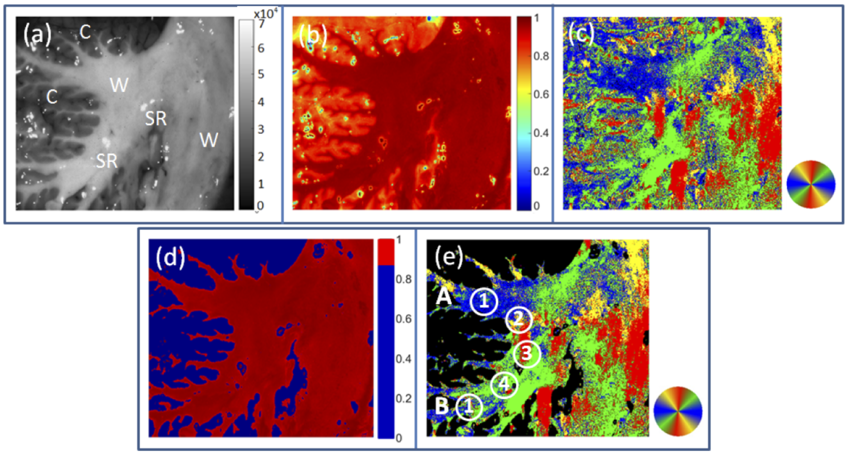

Fig. 2. Coronal cross section of a cadaveric calf cerebellum: a) non-normalized intensity image, C - cortex, W - white matter, SR - specular reflection zones, b) map of depolarization Δ, c) map of azimuth φ, d) binary mask of depolarization Δ generated by using a threshold of $\Delta = 0.85$, e) map of azimuth φ of brain white matter at 550 nm.

The cell-dense cortex consistently shows less depolarization compared to the brain white matter. In order to improve visibility of in-plane fiber tract orientation within the white matter zone we suggest using a mask based on the depolarization threshold ($\Delta < 0.85$) to remove less depolarizing areas of cortex and zones of specular reflection in the images of the azimuth of the optical axis and to highlight the directions of white matter fiber tracts.

Both total intensity and depolarization images demonstrate the contrast between cortex and white matter (Fig. 2(a) and Fig. 2(b)). We observe the orientation of brain white matter fiber tracts in the image of the azimuth of the optical axis (Fig. 2(c)). The zones of cortex demonstrate random orientation of the azimuth at the spatial resolution scale of the IMP system and visually "contaminate" the image, thus, making it difficult to trace brain fibers. The application of the binary mask that contains the pixels with only high values of depolarization allows to filter out the cortex zones and the zones of specular reflection that saturate the CCD camera in the image of the azimuth of the optical axis. An example of binary depolarization mask with a threshold value of $\Delta = 0.85$ is shown in Fig. 2(d). Assuming that all pixels of the azimuth image that demonstrate the depolarization value $\Delta < 0.85$ correspond to cortex zone of brain tissue, we render these pixels in black in the filtered image of the azimuth (Fig. 2(e)). It is worth to note that the zones of the image of the azimuth labelled by (1) and rendered in blue (horizontal orientation), labelled by (2) and rendered in yellow (135° orientation), labelled by (3) and rendered in red (vertical orientation), and labelled by (4) and rendered in green (45° orientation) suggest the presence of in-plane U-fibers connecting the cortical areas (A) and (B) as was shown in [32].

In order to demonstrate the capability of IMP to visualize white matter fiber tracts of a non-fixed brain we prepared a cadaveric calf hemisphere, removing the temporal lobe and large parts of the frontal lobe including the frontal operculum and the insula (see Fig. 3(a)). The intensity image show almost no contrast within the white matter zone apart from the tiny bright regions of specular reflection that is due to uneven surface of the specimen. We applied the depolarization mask with a threshold of $\Delta = 0.85$ for filtering out the cortex zones in the image of the azimuth of the optical axis. Azimuth map reveals a variety of cerebro-spinal (or spino-cerebral) as well as longitudinal tracts - parts of the superior longitudinal fascicle (see Fig. 3(c)).

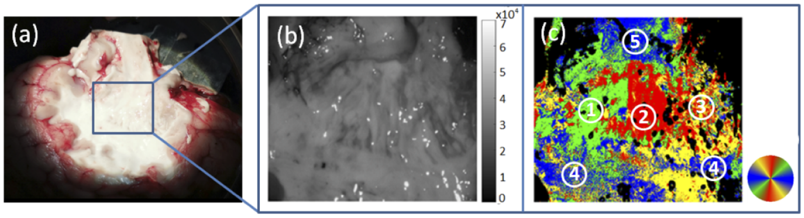

Fig. 3. Cerebral tracts of a cadaveric calf brain: a) photo of a prepared cavity with brain deep white matter tracts. The imaged zone of the size of 3 cm × 3 cm is marked by a blue box; b) intensity image; c) azimuth of the optical axis: the parieto-spinal (label 1, green color), centro-spinal (label 2, red color) and fronto-spinal (label 3, yellow color) tracts; longitudinal tracts (labels 4 and 5, blue color) measured at 550 nm.

3.2. Polarimetric imaging of ex vivo brain sample under adverse conditions

In our prior feasibility tests we took the images of a flat surface of 1 cm thick section of either formalin-fixed human brain or fresh calf brain in the laboratory settings [32]. However, the IMP system is meant for intra-operative use. Uneven surfaces, irrigation fluids and blood might obscure the tissue and negatively impact the capability of our IMP system to identify fiber tracts. We, therefore, tested our system under adverse conditions and applied a depolarization-based mask to the azimuth images in order to filter out the zones of gray matter and specular reflection.

3.2.1. Tilt and rotation of a brain sample

First we imaged the intra-hemispheric corpus callosum (a wide, thick nerve tract, consisting of a flat bundle of fibers, connecting the left and right cerebral hemispheres [42]) of an entire brain that was put in a Petri dish (Fig. 4(a)), and then we tilted a Petri dish by 30° with respect to the imaging plane and imaged a brain sample again (Fig. 4(d)). The intensity images and maps of the azimuth of the optical axis of a corpus callosum are shown in Figs. 4(b), 4(c) and Figs. 4(e), 4(f). The depolarization mask $0.85 < \Delta$ was applied to the azimuth maps to filter out the zones of cortex and specular reflection. As expected, the central horizontal part of a corpus callosum demonstrates vertical orientation of fiber tracts. One should note the presence of the residual fibers of the cingular gyri [42] that are not oriented vertically and obscure the top and bottom zones of a corpus callosum azimuth map. The tilt of a sample is visible in the intensity images as the bright zones of specular reflection seen in the left part of a corpus callosum in the intensity image (Fig. 4(b)) disappear in the corresponding image shown in Fig. 4(e) because of brain sample surface inclination. However, the azimuth of the optical axis of a central part of a corpus callosum is not influenced by sample tilt (Fig. 4(c) and Fig. 4(f)).

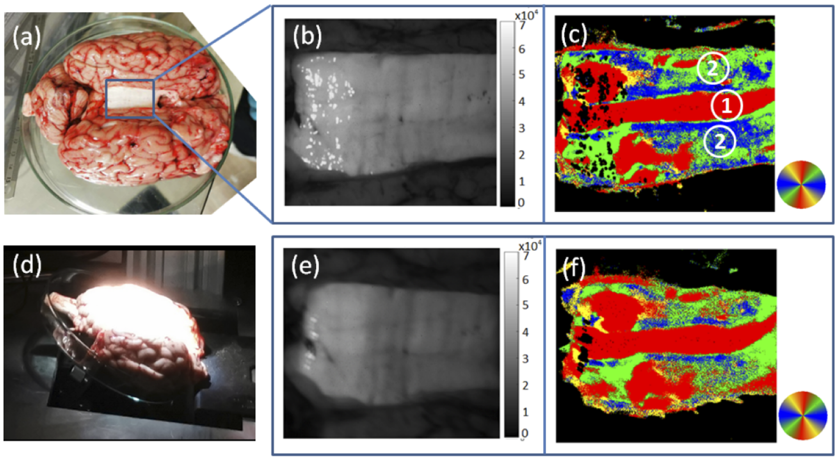

Fig. 4. Images of the corpus callosum in a cadaveric calf brain: a) color photo of a sample, top view; b) intensity image; c) map of the azimuth of the inter-hemispheric corpus callosum, 1) - central part of the corpus callosum, 2) - zones of residual fibers of the cingular gyri. Measurement wavelength is 550 nm, the dimensions of imaged zone are 3cm × 3cm, no tilt; (d) color photo of a tilted sample, side view; (e,f) analogous to (b, c) with a brain sample tilted by 30°. Measurement wavelength is 550 nm.

Then we rotated both tilted and non-tilted brain sample with the step of 45° about the normal to the imaging plane and recorded the Mueller matrices at 550 nm. The maps of the azimuth of the optical axis for both angles of tilt (0° and 30°) and the rotation angles of 0°, 45° and 90° are shown in Fig. 5. The central part of a corpus callosum is rendered in yellow in the azimuth maps recorded for both non-tilted and tilted brain sample at the rotation angle of 45° (Fig. 5(b) and Fig. 5(e)). It corresponds to 45° orientation of the fiber tracts that is consistent with the images in Fig. 5(a) and Fig. 5(d), where the orientation of the corresponding fibers is 90° (i.e. vertical). Accordingly, the central part of a corpus callosum demonstrates horizontal orientation of the fiber tracts for both tilted and non-tilted sample for the rotation angle of 90°. Thus, surface tilt and rotation do not represent a major problem for polarimetric imaging of brain fiber tracts.

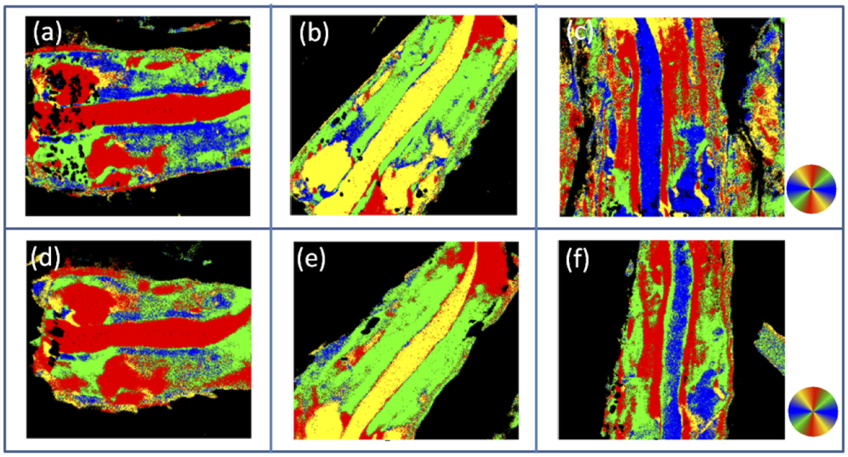

Fig. 5. Maps of the azimuth of the corpus callosum in a cadaveric calf brain measured at 550 nm with no tilt at the rotation angles of a) 0°; b) 45°; c) 0°. The dimensions of imaged zone are 3cm × 3cm; (d-f) analogous to (a-c) with a brain sample tilted by 30°.

3.2.2. Irrigation of a brain sample with saline / blood solution

During open brain neurosurgery the presence of blood within the surgical cavity is a factor that needs to be taken into account when testing the capability of IMP to visualize the brain white matter fiber tracts. We applied blood / saline solutions with different concentrations of blood onto the exposed corpus callosum of a calf brain (Fig. 6). The brain was minimally tilted (5°-10° with respect to the imaging plane) to allow excess blood /saline solution to drain. The residual fibers of the cingular gyri were removed, the saline/blood solutions with the concentration of blood of 10% (which we estimate to most accurately represent intra-operative conditions), 50% (the results are not presented here), and 100% were subsequently applied. The intensity images are slightly affected by the presence of 10% blood solution (Fig. 6(e)), the impact of blood becomes more pronounced for 100% blood solution (Fig. 6(h)). At the same time the presence of blood solution does not influence the maps of the azimuth of the optical axis measured at 550 nm and filtered using depolarization mask for removing the cortex and specular reflection zones (Fig. 6(c) and Fig. 6(f)), and the vertical orientation of a corpus callosum fiber tracts remains visible even after irrigation with 100% blood, as shown in Fig. 6(i).

Next, we created a 2 mm deep pool of undiluted blood by using another piece of brain tissue as a barrier on top of the imaged corpus callosum and preventing blood from draining (Figs. 7(a), 7(d)). The zone of blood is rendered in black in the gray scale image of intensity measured at 550 nm (Fig. 7(b)), but looks more bright in the corresponding image taken at 650 nm (Fig. 7(e)). This is explained by the strong peak of blood hemoglobin absorption at around 550 nm that drops sharply at the wavelength of 650 nm [43]. The previous spatially homogeneous map of the azimuth within the corpus callosum zone was lost for the image recorded at 550 nm (Fig. 7(c)), but the impact of blood on the map of azimuth was mitigated once we switched to 650 nm wavelength of probing light (Fig. 7(f)). Thus, small amounts of spilt blood will not be a major obstacle for intra-operative use of IMP, because surgical cavity is rinsed with a saline solution regularly during neurosurgery.

3.2.3. Impact of complex surface topography

The surgical resection of brain tumor creates a resection cavity, and the area of interest for fiber tract detection with the wide-field IMP might be located within the surgical cavity, and not be

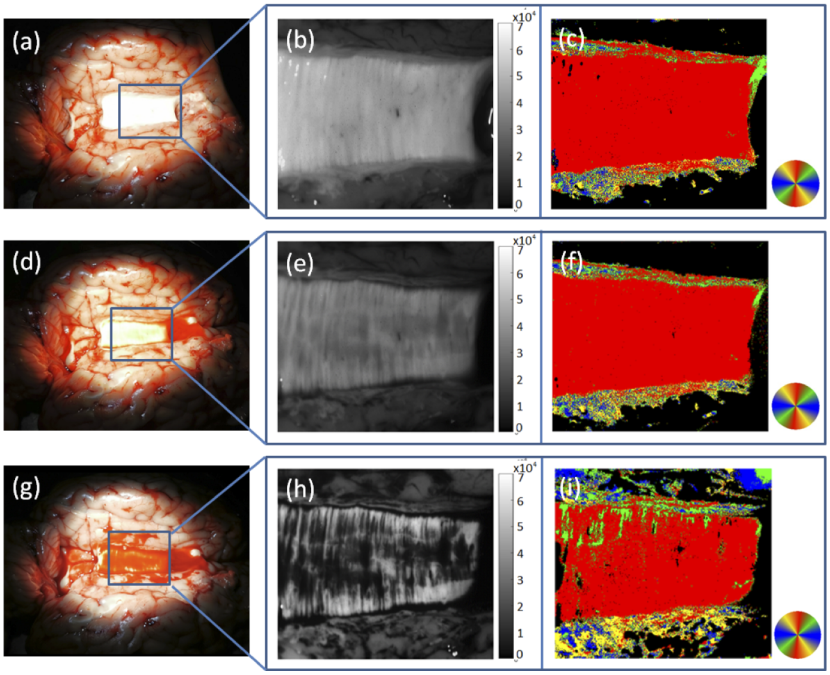

Fig. 6. Top view of the corpus callosum in a cadaveric calf brain following detachment of inter-hemispheric adhesions: a) color photo; b) intensity image; c) map of the azimuth of the optical axis measured at 550 nm. The dimensions of the polarimetric images are 3 cm by 3 cm; (d-f) analogous to (a-c) after sample surface irrigation with a 10% blood solution; (g-i) analogous to (a-c) after sample surface irrigation with undiluted blood.

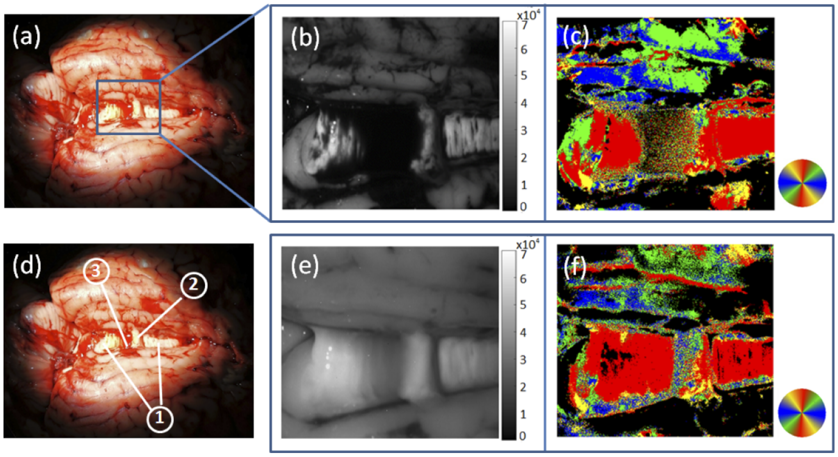

Fig. 7. Images of the corpus callosum in a cadaveric calf brain with a 2 mm deep pool of 100% blood: a) color photo; b) intensity image; c) azimuth of the optical axis measured at 550 nm; d) corpus callosum (1) with a ~ 2 mm thick tissue specimen (2) creating a 2 mm deep pool of whole blood (3); e) intensity image and f) azimuth of the optical axis measured at 650 nm.

on a flat surface. Thus, in order to mimic *in vivo* conditions we performed IMP measurements in a 2 cm deep resection cavity in a calf brain sample (see Fig. 8). The depolarization mask 0.85<Δ was applied to the azimuth map to filter out the zones of cortex and specular reflection. The dimension of the imaged zone is 3 cm × 3 cm, the wavelength of measurements is 550 nm. The image of the azimuth of the optical axis demonstrates clearly in-plane orientation of the thick fiber tracts that is consistent with the anatomy of this brain section. Hence, the quality of visualization of fiber tracts and their orientation with the wide-field IMP measurements within a cavity did not seem inferior to the measurements on a flat surface.

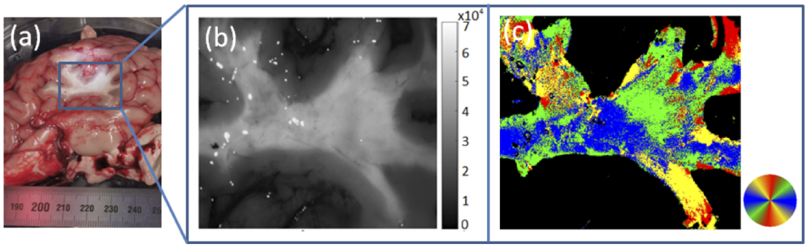

Fig. 8. A 2 cm deep cavity was made with sharp instruments onto a cadaveric calf brain: a) photo of a brain sample; b) intensity image of the central part of cavity; c) azimuth of the optical axis measured at 550 nm.

4. Conclusions

The proposed approach for the visualization of fiber tracts of healthy brain white matter using the multi-spectral wide-field IMP offers a non-invasive, staining-free, fast and reproducible method for identifying tumor margins by detecting in-plane fiber orientation during brain surgery. The correlation of the direction of brain fiber tracts with the orientation of the optical axis of linear birefringent medium measured with IMP modality was proven with the gold standard histology analysis of silver-stained thin sections of brain tissue [32]. Thus, we believe that the wide-field IMP technique has the potential to detect the precise border between optically anisotropic healthy brain white matter and isotropic brain tumor tissue, to increase the extent of resection in surgery on all intrinsic brain tumors, especially on low-grade glioma of young people, for which the current technologies have significant limitations and drawbacks, and to further decrease surgical morbidity.

Further studies are envisaged for the polarimetric imaging of freshly excised brain tumor specimens, especially the ones that may contain both tumor and healthy tissue to prove the validity of our hypothesis and relevance of IMP approach in near *in vivo* clinical settings.

Funding. Ecole Polytechnique, Institut Polytechnique de Paris; Consejo Nacional de Ciencia y Tecnología (CVU 482980).

Acknowledgments. We thank Andrea Mathis for scientific coordination, as well as Irena Zubak, Michael Murek and Johannes Goldberg for running the HORAO crowdfunding and crowdsourcing campaigns.

Disclosures. The authors declare no conflicts of interest.

Data availability. Data underlying the results presented in this paper are not publicly available at this time but may be obtained from the authors upon reasonable request.

References

1. AWMF online, Clinical Practice Guidelines, https://www.awmf.org/en/clinical-practice-guidelines.html.
2. P. Schucht, J. Beck, and K. S. K A. Raabe, "Extending resection and preserving function: modern concepts of glioma surgery," Swiss Med. Wkly. **145**, w14082 (2015).
3. P. Roth, A. F. Hottinger, T. Hundsberger, H. Läubli, P. Schucht, M. Reinert, C. Mamot, U. Roelcke, G. Pesce, S. Hofer, and M. Weller, "A contemporary perspective on the diagnosis and treatment of diffuse gliomas in adults," Swiss Med. Wkly. **150**, w20256 (2020).

4. M. Rahman, J. Abbatematteo, E. K. D. Leo, P. S. Kubilis, S. Vaziri, F. Bova, E. Sayour, D. Mitchell, and A. Quinones-Hinojosa, "The effects of new or worsened postoperative neurological deficits on survival of patients with glioblastoma," J. Neurosurg. **127**(1), 123–131 (2017).
5. A. W. Awad, M. Karsy, N. Sanai, R. Spetzler, Y. Zhang, Y. Xu, and M. A. Mahan, "Impact of removed tumor volume and location on patient outcome in glioblastoma," J Neurooncol. **135**(1), 161–171 (2017).
6. Y. Rho, S. Rhim, and J. Kang, "Is intraoperative neurophysiological monitoring valuable predicting postoperative neurological recovery?" Spinal Cord. **54**(12), 1121–1126 (2016).
7. G. Bertani, E. Fava, G. Casaceli, G. Carrabba, A. Casarotti, C. Papagno, A. Castellano, A. Falini, S. M. Gaini, and L. Bello, "Intraoperative mapping and monitoring of brain functions for the resection of low-grade gliomas: technical considerations," Neurosurg. Focus. FOC **27**(4), E4 (2009).
8. G. M. Ibrahim and M. Bernstein, "Awake craniotomy for supratentorial gliomas: why, when and how?" CNS Oncol. **1**(1), 71–83 (2012).
9. G. Herbet, "Should complex cognitive functions be mapped with direct electrostimulation in wide-awake surgery? anetwork perspective," Front. Neurol. **12**, 521 (2021).
10. L. H. Stieglitz, J. Fichtner, R. Andres, P. Schucht, A. Krähenbühl, A. Raabe, and J. Beck, "The silent loss of neuronavigation accuracy: A systematic retrospective analysis of factors influencing the mismatch of frameless stereotactic systems in cranial neurosurgery," Neurosurgery **72**(5), 796–807 (2013).
11. P. Schucht, S. Knittel, J. Slotboom, K. Seidel, M. Murek, A. Jilch, A. Raabe, and J. Beck, "5-ALA complete resections go beyond MR contrast enhancement: Shift corrected volumetric analysis of the extent of resection in surgery for glioblastoma," Acta Neurochir. **156**(2), 305–312 (2014).
12. L. Alston, L. Mahieu-Williame, M. Hebert, P. Kantapareddy, D. Meyronet, D. Rousseau, J. Guyotat, and B. Montcel, "Spectral complexity of 5-ALA induced PpIX fluorescence in guided surgery: a clinical study towards the discrimination of healthy tissue and margin boundaries in high and low grade gliomas," Biomed. Opt. Express **10**(5), 2478–2492 (2019).
13. T. Novikova, "Optical techniques for cervical neoplasia detection," Beilstein J. Nanotechnol. **8**, 1844–1862 (2017).
14. E. Errichetti and G. Stinco, "Dermoscopy in general dermatology: A practical overview," Dermatol Ther (Heidelb) **6**(4), 471–507 (2016).
15. S. J. Bonsor, "The use of the operating microscope in general dental practice. part 2: If you can see it, you can treat it!" Dent Updat. **42**(1), 60–66 (2015).
16. L. Han, Z. Hosseinaee, E. L. Irving, D. Hileeto, C. Chan, and K. K. Bizheva, "Imaging the fibrous structure of the ocular sclera with UHR-OCT," Invest. Ophthalmol. & Visual Sci. **60**, 1299 (2019).
17. M. Akarsu and C. Akarsu, "Evaluation of new technologies in gastrointestinal endoscopy," J Soc Laparosc. Robotic Surg. **22**(1), e2017.00053 (2018).
18. J. Jonkman, C. M. Brown, G. D. Wright, K. I. Anderson, and A. J. North, "Tutorial: guidance for quantitative confocal microscopy," Nat. Protoc. **15**(5), 1585–1611 (2020).
19. A. M. Zysk, F. T. Nguyen, A. L. Oldenburg, D. L. Marks, and S. A. Boppart, "Optical coherence tomography: a review of clinical development from bench to bedside," J. Biomed. Opt. **12**(5), 051403 (2007).
20. L. Marcu, J. A. Jo, P. V. Butte, W. H. Yong, B. K. Pikul, K. L. Black, and R. C. Thompson, "Fluorescence lifetime spectroscopy of glioblastoma multiforme," Photochem. Photobiol. **80**(1), 98–103 (2004).
21. D. H. Goldstein, *Polarized light* (3rd ed. CRC Press, 2010).
22. H. R. Lee, I. Saytashev, V. N. Du Le, M. Mahendroo, J. C. Ramella-Roman, and T. Novikova, "Mueller matrix imaging for collagen scoring in mice model of pregnancy," Sci. Rep. **11**(1), 15621 (2021).
23. S. L. Jacques, J. C. Ramella-Roman, and K. Lee, "Imaging skin pathology with polarized light," J. Biomed. Opt. **7**(3), 329–340 (2002).
24. T. Novikova, A. Bénière, F. Goudail, and A. De Martino, "Sources of possible artefacts in the contrast evaluation for the backscattering polarimetric images of different targets in turbid medium," Opt. Express **17**(26), 23851 (2009).
25. M. Menzel, M. Axer, K. Amunts, H. De Raedt, and K. Michielsen, "Diattenuation imaging reveals different brain tissue properties," Sci. Rep. **9**(1), 1939 (2019).
26. A. Jain, L. Ulrich, M. Jaeger, P. Schucht, M. Frenz, and H. G. Akarzay, "Backscattering polarimetric imaging of the human brain to determine the orientation and degree of alignment of nerve fiber bundles," Biomed. Opt. Express **12**(7), 4452–4466 (2021).
27. C. Fallet, T. Novikova, M. Foldyna, S. Manhas, B. Haj Ibrahim, A. De Martino, C. Vannuffel, and C. Constancias, "Overlay measurements by Mueller polarimetry in back focal plane," J. Micro/Nanolith. MEMS MOEMS **10**(3), 033017 (2011).
28. T. Novikova and P. Bulkin, "Inverse problem of Mueller polarimetry for metrological applications," J. Inverse Ill-Posed Probl. (), 000010151520200140 (2021). doi:10.1515/jiip-2020-0140.
29. J. Vizet, J. Rehbinder, S. Deby, S. Roussel, A. Nazac, R. Soufan, C. Genestie, C. Haie-Meder, H. Fernandez, F. Moreau, and A. Pierangelo, "In vivo imaging of uterine cervix with a Mueller polarimetric colposcope," Sci. Rep. **7**(1), 2471 (2017).
30. I. Meglinski, L. Trifonyuk, V. Bachinsky, O. Vanchulyak, B. Bodnar, M. Sidor, O. Dubolazov, A. Ushenko, Y. Ushenko, I. V. Soltys, A. Bykov, B. Hogan, and T. Novikova, *Shedding the Polarized Light on Biological Tissues* (Springer, 2021).

31. A. Vitkin, N. Ghosh, and A. De Martino, "Tissue polarimetry," in *Photonics: Biomedical Photonics Spectroscopy, and Microscopy*, D. L. Andrews, ed. (John Wiley & Sons, Inc., 2015).
32. P. Schucht, H. R. Lee, M. H. Mezouar, E. Hewer, A. Raabe, M. Murek, I. Zubak, J. Goldberg, E. Kövari, A. Pierangelo, and T. Novikova, "Visualization of white matter fiber tracts of brain tissue sections with wide-field imaging Mueller polarimetry," IEEE Trans. Med. Imaging **39**(12), 4376–4382 (2020).
33. S. Y. Lu and R. A. Chipman, "Interpretation of Mueller matrices based on polar decomposition," J. Opt. Soc. Am. A **13**(5), 1106–1113 (1996).
34. T. Novikova, J. Rehbinder, H. Haddad, S. Deby, B. Teig, A. Nazac, A. Pierangelo, F. Moreau, and A. D. Martino, "Multi-spectral Mueller matrix imaging polarimetry for studies of human tissue," OSA Biophotonics Congress, Clinical and Translational Biophotonics, paper TTh3B (2016).
35. M. Kupinski, M. Boffety, F. Goudail, R. Ossikovski, A. Pierangelo, J. Rehbinder, J. Vizet, and T. Novikova, "Polarimetric measurement utility for pre-cancer detection from uterine cervix specimens," Biomed. Opt. Express **9**(11), 5691–5702 (2018).
36. M. Borovkova, A. Bykov, A. Popov, A. Pierangelo, T. Novikova, J. Pahnke, and I. Meglinski, "Evaluating β-amyloidosis progression in Alzheimer's disease with Mueller polarimetry," Biomed. Opt. Express **11**(8), 4509 (2020).
37. M. Peyvasteh, A. Popov, A. Bykov, A. Pierangelo, T. Novikova, and I. Meglinski, "Evolution of raw meat polarization-based properties by means of Mueller matrix imaging," J. Biophotonics **14**(5), e202000376 (2021).
38. A. Lindberg, J. Vizet, J. Rehbinder, C. Gennet, J. C. Vanel, and A. Pierangelo, "Innovative integrated numerical-experimental method for high-performance multispectral mueller polarimeters based on ferroelectric liquid crystals," Appl. Opt. **58**(19), 5187–5199 (2019).
39. E. Compain, S. Poirier, and B. Drévillon, "General and self-consistent method for the calibration of polarization modulators, polarimeters, and Mueller-matrix ellipsometers," Appl. Opt. **38**(16), 3490–3502 (1999).
40. N. Ghosh and A. Vitkin, "Tissue polarimetry: concepts, challenges, applications, and outlook," J. Biomed. Opt. **16**(11), 110801 (2011).
41. S. Jimsheleishvili and M. Dididze, "Neuroanatomy, cerebellum," in *StatPearls [Internet]*, (StatPearls Publishing, Treasure Island (FL), 2021). https://www.ncbi.nlm.nih.gov/books/NBK538167/.
42. B. A. Vogt, E. A. Nimchinsky, L. J. Vogt, and P. R. Hof, "Human cingulate cortex: Surface features, flat maps, and cytoarchitecture," J. Comp. Neurol. **359**(3), 490–506 (1995).
43. S. Prahl, "Optical absorption of hemoglobin," 1999 Portland, OR: Oregon Med. Laser Center. [Online], http://omlc.ogi.edu/spectra/hemoglobin/.